Hybrid Cellular Automaton - Parabolic Thick Needle model for equiaxed dendritic solidification

Romain Fleurisson, Oriane Senninger, Gildas Guillemot, Charles-André Gandin

Hybrid Cellular Automaton - Parabolic Thick Needle model for equiaxed dendritic solidification

Romain Fleurisson, Oriane Senninger, Gildas Guillemot*, Charles-André Gandin

MINES ParisTech, PSL Research University, CEMEF UMR CNRS 7635, CS10207, 06904 Sophia Antipolis, France

Abstract

A hybrid Cellular Automaton (CA) - Parabolic Thick Needle (PTN) model is developed for the simulation of an equiaxed dendritic grain. It is implemented by solving conservation equations with the Finite Element (FE) method at two scales. At the scale of the microstructure, dendritic branches are approximated by a network of PTN. The solute field is computed in the liquid using a FE mesh with minimum size smaller than the diffusion length ahead of the dendrite tips, giving access to a detailed description of each dendrite tip growth velocity as well as solutal interactions between branches. At the simulation domain scale, volume averaged heat and solute transfers are solved on a coarser FE mesh. The average volumetric fraction of phases is deduced from a field giving the fraction of dendritic microstructure together with a microsegregation model. Because the PTN themselves grow on CA cells, the dendrite tip growth velocity is transferred to the vertices of the polygon associated to the CA growth shape. Similarly, the field giving the fraction of dendritic microstructure is deduced from the fraction of CA cells part of the mushy zone, which include cells containing PTN network. Advantages of the new multiple scale CAPTN model include solutal interaction between dendrite branches together with long range transfer of heat and solute mass, together with the role of latent heat release on equiaxed solidification.

Keywords: Solidification, Dendrite growth law, Multiscale, Finite Element method

Nomenclature

Latin symbols

a	Integration parameter	m
d_0	Capillary length	m
g	Volume fraction	$m^3.m^{-3}$

*Corresponding author
Email address: Gildas.Guillemot@mines-paristech.fr (Gildas Guillemot)

h_{min}	Minimum mesh size	m
h_{max}	Maximum mesh size	m
k	Segregation coefficient	wt%.wt%$^{-1}$
l_{CA}	Cell size	m
l_{ν}^{i}	Length of branch i of polygon in cell ν	m
m	Liquidus slope	K.wt%$^{-1}$
r_{cyl}	Truncation radius	m
t	Time	s
v	Velocity	m.s^{-1}
w	Composition	wt%
p^s	Factor on solid PTN mesh size	-
C_p	Volumetric heat capacity	J.K^{-1}.m^{-3}
D^l	Diffusion coefficient of the liquid phase	m^2.s^{-1}
$\mathcal{F}$	Flux intensity factor	-
H	Volumetric enthalpy	J.m^{-3}
L_M	Volumetric latent heat	J.m^{-3}
T	Temperature	K

Greek symbols

δ^s	Boolean field of the solid phase in the PTN mesh	-
δ^{ls}	Boolean field of the liquid-solid interface in the PTN mesh	-
κ	Thermal conductivity	W.m^{-1}.K^{-1}
ρ	Curvature radius	m
σ	Selection parameter	-
Δt	Time step	s
ΔT	Undercooling	K
Γ^{ls}	Gibbs-Thomson coefficient	K.m

Ω	Supersaturation	-

Superscripts

s	solid phase
l	liquid phase
ls	liquid-solid interface
m	mushy zone

Subscripts

eut	Eutectic
lim	Threshold value
tip	Related to a dendrite tip parabola
FE	Field on the FE mesh
Iv	Related to the Ivantsov solution
M	Melting
PTN	Field on the PTN mesh

1. Introduction

Solidification processing of metallic alloys involves highly multi-physical phenomena acting over a broad range of time and space scales. This multiscale complexity makes simulation of solidification challenging and leads to the use of specific simplifying hypotheses depending on the scale of the simulated domain [1].

The Cellular Automaton method (CA) was initially developed for the simulation of the grain structure generated by primary dendritic solidification in casting [2]. The grain structure is modelled by a set of CA cells with the same grain index. For cells located at the boundary with the liquid, a growth algorithm is applied that makes use of a dendrite tip growth kinetics model [2] and assume development of the dendrite trunks and branches along the $< 100 >$ crystallographic directions for cubic metals [3, 4, 5]. Within the grain, a mushy zone is present that progressively solidifies upon cooling, characterized by a distribution of solid and liquid phases and their composition [6]. It has been shown that simulation of the grain structure with the CA method can easily be applied to components typical of shape casting [7, 8, 9]. To reach this objective, two main approximations are considered, offering alternatives to the detailed description of the dendritic microstructure and its associated mushy zone.

Because dendritic growth is mainly controlled by solute redistribution between the solid and liquid phases and chemical diffusion in the liquid phase, a dendrite tip kinetics model requires to know the local composition field in the liquid ahead of the solid-liquid interface. This is yet not directly simulated using the CA method but approximated by the analytical steady state composition profile around a paraboloidal solid-liquid interface representing the dendrite tip shape [10]. Together with the marginal stability criterion [11], it provides with a dendrite tip growth law which accounts for the average composition, local temperature and even fluid flow [12]. One should note that the average composition is not necessarily the alloy composition when large scale redistribution of solute takes place. This is the case in the presence of macrosegregation due to the convective transport of phases [13, 9, 14]. Similarly, the mushy zone created by the intricate complexity of the dendritic morphology is not directly simulated. Instead, the method of volume averaging is applied to the conservation equations [15, 16]. This requires introducing a microsegregation law to describe the average volume fraction of phases, the simplest description being given by the classical lever rule and Gulliver-Scheil solidification paths [6] that can be deduced from thermodynamic information [17]. Solving the average conservation equation with the Finite Element (FE) method and coupling with the CA method lead to the so-called CA-FE model. The advantage of this construction is to reach large scale simulation domains with a direct description of the grain structure and full coupling with heat, solute and momentum conservations, yet not directly simulating the dendritic microstructure. The CA method was further developed for the prediction of the dendritic microstructure itself [18, 19, 20, 21]. In principle this provides an alternative to the phase field (PF) method developed to provide a quantitative solution to solute redistribution at the solid-liquid interface while relying on a sound description of the interfacial phenomena, including curvature and anisotropic interfacial energy [22]. The phase field method is yet often limited to small simulation domains, even with the advent of High Performance Computing (HPC) including the use of multiple Graphics Processing Unit (GPU) [23, 24]. But extensions of the CA method for direct simulation of the dendritic microstructure reach similar limitations as the smallest scale to be resolved for quantitative prediction is the dendritic tip radius (typically less than a micrometer). The claim of the authors is that simplifications are possible with respect to heat transfers, reducing the heat flow to an imposed temperature field. One can also note that little effort is available to validate these extensions of the CA method to predict dendritic microstructure by comparing them to phase field simulations. Yet the latter numerical developments of PF including HPC and GPU have led to the possibility to conduct heavy simulations and comparisons with the CA method applied to columnar dendritic growth, thus quantifying the consequence of the built-in approximations on grain selection maps [25]. Comparisons were yet still limited to two dimensional (2D) PF simulations with an imposed temperature field.

New methodologies have been developed for simulation of dendritic growth, always with the need to reach larger scale simulations than currently available with PF. They are referred to as mesoscopic mod-

els [26, 27, 28, 29, 30, 31, 32]. The objective is similar to the extensions of the CA method with the goal to perform direct growth simulation of the dendritic microstructure. The Dendritic Needle Network (DNN), the Parabolic Thick Needle (PTN) and the Grain Envelope Model are good examples. These models solve the solute diffusion problem over a range of length scales ranging from the dendrite tip radius to an ensemble of dendritic grains. Hence, they are relevant to compute the dendrite tip velocity, the interaction of the solute field between dendrites and the grain growth in non-stationary situations. However, from the best of our knowledge, these models have not been coupled to heat flow and are only used with an imposed temperature history.

The objective of the present contribution is to combine the CA and the PTN methods in a new dendritic grain model while maintaining the coupling with the FE solutions of heat and mass transfers. The 2D implementation described hereafter lays the foundation of the coupling and evaluates its inputs and outputs compared to the CA-FE model. The implementation of the PTN method is explained, followed by a description of its coupling with the CA method to gain a non-steady-state CAPTN dendrite growth model. Application is given for the Al-7wt%Si alloy. The influence of numerical parameters is evaluated along with its ability to compute dendritic growth for a large range of supersaturation. The full CAPTN-FE model is then tested and compared to the CA-FE model to demonstrate non stationary dendrite tip growth due to both the solute diffusion field in the liquid and coupling with heat flow, as well as mushy zone solidification.

2. Modeling

2.1. Parabolic Thick Needle (PTN) model

2.1.1. Principle

The PTN method is introduced for the computation of the dendrite tip kinetics as part of the DNN model introduced by Tourret and Karma [26, 27]. It represents a dendrite tip as a parabola with radius ρ_{tip}. The parabola is further truncated by a cylinder of radius r_{cyl} as schematized in Fig. 1. To compute the growth of a dendrite tip, solute diffusion is solved in the liquid phase to obtain the concentration field w^l_{PTN}:

$$\frac{\partial w^l_{PTN}}{\partial t} - D^l \Delta w^l_{PTN} = 0 \tag{1}$$

where D^l is the interdiffusion coefficient in the liquid phase. The concentration field at the solid-liquid interface is imposed to the equilibrium interface concentration w^{ls} associated to the temperature of the tip. Tourret and Karma [27] also note that on a time scale much smaller than the diffusion time scale, the growth of dendritic branches could be considered as quasi-stationary with stable curvature radius ρ_{tip} and a constant growth velocity v_{tip} along the growth direction. To compute the growth velocity v_{tip} and

the curvature radius of dendrite tips, the PTN model uses two relations. The first one is the solvability condition [33, 34] giving:

$$\rho_{tip}^2 v_{tip} = \frac{D^l d_0}{\sigma} \tag{2}$$

where σ is the dendrite tip selection parameter, which is supposed to only depend on the alloy system and the growing phase. The d_0 parameter is the capillary length. Assuming a linearized phase diagram with liquidus slope m and segregation coefficient k, this parameter writes $d_0 = -\Gamma^{ls}/m(1-k)w^{ls}$, where Γ^{ls} is the Gibbs-Thomson coefficient defined for the solid-liquid interface. It has to be noted that different versions of Eq. (2) appear in the literature (with or without a factor of 2 on the right-hand-side). A discussion on the choice made here can be found in [25].

The second relation is associated to the integration of the conservation equation at the solid/liquid interface in the vicinity of the tips. On this time scale, it is assumed that the parabola grows in a

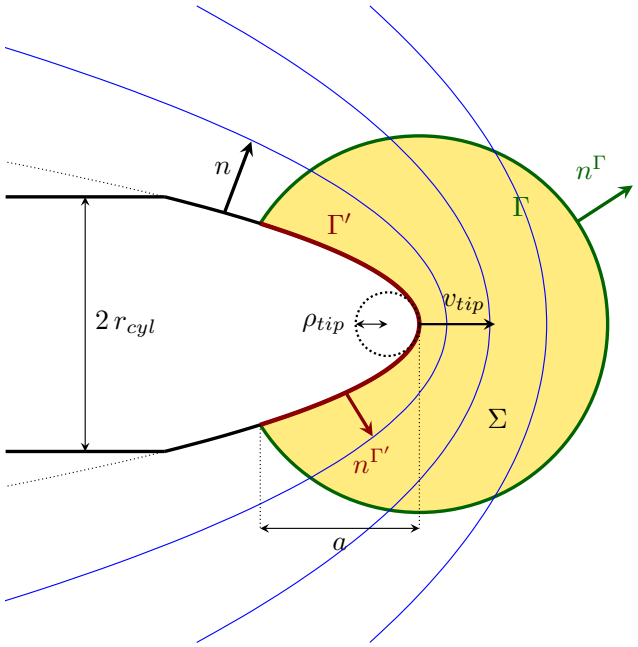

Figure 1: Parabolic dendrite tip of curvature ρ_{tip} and growth velocity v_{tip} truncated by a cylinder of radius r_{cyl}. The yellow area of surface Σ is parametrized by the length a defining a distance behind the tip of the parabola. Blue lines correspond to iso-values of the concentration field in the liquid phase w^l_{PTN} computed by solving Eq. (1).

stationary state, which permits to approximate the dendrite velocity to its displacement velocity $\mathbf{v_{tip}}$ with no variation of the radius ρ_{tip}. In addition, the concentration field is supposed to behave as a quasi-stationary state. Assuming that diffusion is negligible in the solid phase and that the solid and the liquid phases have the same density, the balance of the solute flux at solid-liquid interface of the dendrite

tip writes:

$$\frac{-D^l}{(1-k)w^{ls}}\nabla w^l_{PTN}\mid^{ls}\cdot\mathbf{n}=\mathbf{v_{tip}}\cdot\mathbf{n} \tag{3}$$

The integration of Eq. (3) on the Γ' contour parametrized by the length a (see Fig. 1) gives [27]:

$$\rho_{tip}v_{tip}^2=\frac{2\ D^{l2}\mathcal{F}^2}{d_0} \tag{4}$$

where the flux intensity factor $\mathcal{F}$ is defined by:

$$\mathcal{F}=\frac{-1}{4\sqrt{a/d_0}(1-k)w^{ls}}\int_{\Gamma'}\nabla w^l_{PTN}\mid^{ls}\cdot\mathbf{n}\mathrm{d}\Gamma' \tag{5}$$

The solution of Eq. (2) and (4) provides access to both the growth velocity and the curvature radius of the dendrite tip as long as the flux intensity factor is correctly estimated in the vicinity of the dendrite tip. Appendix A demonstrates that the analytical solution of the concentration field around a parabolic tip in steady state growth, known as the Ivantsov solution [10], is a solution of Equations (4) and (5) at steady state.

2.1.2. Numerical implementation

The original PTN model has been implemented by Tourret and Karma [26, 27] using the finite difference method. In the present work, the FE method is used together with an adaptive mesh latter referred to as "PTN mesh". It is therefore possible to have a fine resolution of the concentration field close to dendrite tips and to limit numerical cost by using a larger mesh size far from the interface. However, a very fine mesh on the Γ' contour is required to compute the flux intensity factor $\mathcal{F}$ with a good precision using Eq. (5). In order to avoid this numerical cost, Eq. (5) is transformed in two integrals [26, 27] respectively associated to the Γ contour and Σ surface, using the Green-Ostrogradski theorem:

$$\mathcal{F}\approx\frac{-1}{4\sqrt{a/d_0}(1-k)w^{ls}}\left(\int_{\Gamma}\nabla w^l_{PTN}\cdot\mathbf{n}\mathrm{d}\Gamma+\frac{1}{D^l}\iint_{\Sigma}\mathbf{v_{tip}}\cdot\nabla w^l_{PTN}\mathrm{d}\Sigma\right) \tag{6}$$

Two boolean fields are defined to indicate which FE nodes are inside the parabola, δ^s, and in the liquid but at the interface, δ^{ls}. Note that a triangular mesh is used that does not conform to the parabola interface. Determining if a node is within the parabola is straightforward, leading to the condition $\delta^s=1$. Nodes in the liquid at the vicinity of the interface belong to a triangular element with at least one node with $\delta^s=1$. The equilibrium concentration w^{ls} associated to the tip temperature is imposed at the nodes within the parabola, i.e. for which $\delta^s=1$. Equation (1) is then solved on the PTN mesh using this Dirichlet condition to compute the concentration field w^l_{PTN}. In this model, the minimum mesh size h_{min} is imposed in the vicinity of the solid-liquid interface. Inside the truncated parabola, the mesh size

is set to $p^s h_{min}$ where p^s is an integer. For nodes in the liquid, an anisotropic mesh depending on the local concentration field is created. To construct this mesh, a geometric error estimator [35] is used to build a metric with eigenvalues Λ computed as:

$$\Lambda = \min\left(\max\left(\frac{c}{\epsilon}\left|\lambda\right|, \frac{1}{h_{max}^2}\right), \frac{1}{h_{min}^2}\right) \tag{7}$$

were $c = \frac{1}{2}(\frac{d}{d+1})^2$ with d the space dimension, ϵ a maximal interpolation error, λ the eigenvalues of the concentration Hessian matrix, and h_{max} the maximal mesh size prescribed. A remeshing is performed each time a parabola has grown over more than one element since the last remeshing or each time a new parabola is created (see section 2.2).

2.2. Cellular Automaton-Parabolic Thick Needle model

The PTN growth law described in previous section 2.1 determines the growth velocity v_{tip} of the dendrite tip at each time increment. This growth law is introduced in the CA method to compute the envelope of a grain in the solidifying domain. The CA methodology is first presented, followed by a description of the coupling.

2.2.1. Principle of the CA method

The CA method is based on the subdivision of the solidifying domain in a regular grid of square cells of size l_{CA}. At cell scale, the dendritic branches are approximated by a polygon whose perpendicular axes correspond to the $< 100 >$ preferred dendritic growth directions. Fig. 2a presents a CA grid and a polygon (in red) of vertices S_ν^i and length l_ν^i with $i = \{0..3\}$ associated to the central cell labelled ν. The center of the polygon is not necessarily located at the cell center as explained elsewhere [5]. For each time step Δt, branch growth velocity v_{tip} is determined thanks to a growth law (see detailed explanation on computation of v_{tip} in section 3.2.2) and polygon axes are increased by $v_{tip}\ \Delta t$. The dendritic branches will propagate in the cellular grid by the capture of neighboring cells by the growing polygon. When a neighboring cell μ is captured (method detailed in section 2.2.2) by the polygon associated to cell ν, a new polygon is initialized for cell μ with the same orientation as the polygon of capture (in green in Fig. 2b). When all neighbors of a given cell ν contain a growing polygon, the development of the polygon associated to cell ν is stopped and the cell is deallocated from the memory. Note that a maximum length for all $< 100 >$ directions is also prescribed to the polygon, proportional to the cell size l_{CA}, as propagation of the dendritic branches can only take place to capture the neighboring cells. This capture algorithm propagating the dendritic branches at velocity v_{tip} and in a unique set of preferred $< 100 >$ directions defines the growth of the envelope of a single grain.

2.2.2. Coupling PTN to the CA method

The principle of the coupling is to compute branch velocities at CA cell scale using the PTN solution. To do so, a PTN mesh is superimposed to the cellular automaton grid, and a parabola is associated to each polygon tip on the PTN mesh (see Fig. 2a). The list of polygon velocities $\{v_{tip,k}\}$ is therefore

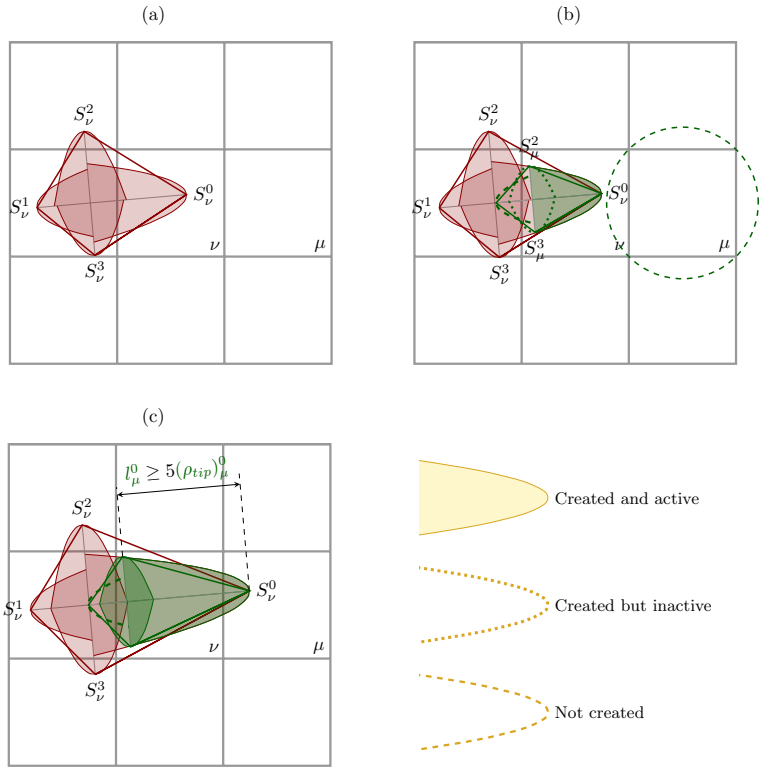

Figure 2: Illustration of the coupling between the CA and the PTN method. Initialization of a polygon after the capture of a cell μ by the polygon of cell ν.

computed on the PTN mesh using concentration gradients deduced from the w_{PTN}^l field in the vicinity of parabolic tips according to the description given in section 2.1 (see additional explanations is section 3.2.2).

To perform cell captures, a circumscribed circle is attached to each cell of the CA grid (Fig. 2b). As the polygon of cell ν enters into the circumscribed circle of a neighboring cell μ by a tip or a side, the neighboring cell is "captured" by the polygon (Fig. 2b). The branch of the capturing polygon closer to the captured cell center is identified as the capturing branch '*cb*'.

Branch lengths l_μ^i and parabolae of the new polygon have then to be initialized. For this, the side of the capturing polygon, of length L_ν^{capt}, which performs the capture is identified by analyzing the position of the center of the captured cell against the capturing polygon. In Fig. 2, the capturing side is $S_\nu^3 S_\nu^0$ as

the center of cell μ is located at south-east of the capturing polygon. The branch '*cb*' of the new polygon associated to cell μ is initialized to $L_\nu^{capt}/2$ and its parabola is defined with the same curvature radius and the same velocity as the one of the capturing branch. The length of the opposite branch is rescaled on the opposite branch of the capturing polygon by a factor $L_\nu^{capt}/2l_\nu^{cb}$. As the branch opposite to the branch of capture is a fictitious branch, the parabola associated to this branch is not created and thus, this branch is not allowed to grow. This branch will be called in the following the "internal branch". Lengths of adjacent branches are initialized to the minimum value between the thickness of the parabola associated to the capturing branch '*cb*' and the truncation radius r_{cyl}. In order to avoid to hinder the growth of the main branch, these branches are only allowed to grow after the branch '*cb*' has reached a length higher than five times its curvature radius (Fig 2c). In this case, adjacent branches lengths are rescaled on the thickness of the branch '*cb*' parabola or to its truncation radius r_{cyl}. Their curvature radii are then initialized to the one of branch '*cb*' and their growth velocities are set to zero before being computed from the local concentration field w_{PTN}^l.

2.3. Coupling the CAPTN approach to the FE model of heat and mass transfers

Until now, the PTN model described in literature has permited to model structures of solidification for imposed temperature fields. The CA-FE model gives the possibility to couple grain structures with energy and solute conservation equations at a larger scale. This coupling can be generalized to the CAPTN model as a multiscale CAPTN-FE model. In a first part, a recall of the classical CA-FE approach is given. The specificities of the CAPTN-FE model are detailed in a second part.

2.3.1. Recall on the CA-FE model

The principle of the CA-FE model has been previously described in the literature [36, 8]. Here, only a summary of this model is given. The solution of conservation equations is performed at the macroscopic scale of the solidifying domain. To do so, the volume averaging technique is used [37]. For each Representative Elementary Volume (REV) of volume V, quantities ξ are averaged as $\langle\xi\rangle = \left(\int_V \xi dV\right)/V$. This REV can contain several phases ϕ for which the ξ quantity has an average intrinsic value $\langle\xi\rangle^\phi$, i.e. averaged over volume V^ϕ of the phase ϕ. Therefore, the average quantity $\langle\xi\rangle$ can be written as:

$$\langle\xi\rangle = \Sigma_\phi g^\phi \langle\xi\rangle^\phi \tag{8}$$

where g^ϕ is the volume fraction of phase ϕ in the REV. With the above notation, the volume averaging method is applied to describe energy and solute mass conservation for a two-phase system made of solid and liquid. In the absence of convection, one can write:

$$\frac{\partial \langle H \rangle}{\partial t} - \langle \kappa \rangle \Delta T = 0 \tag{9a}$$

$$\frac{\partial \langle w \rangle_{FE}}{\partial t} - \nabla.(D^l g^l \nabla \langle w^l \rangle^l_{FE}) = 0 \tag{9b}$$

where $\langle H \rangle$ is the average volumetric enthalpy, $\langle \kappa \rangle$ is the average thermal conductivity, $\langle w \rangle_{FE}$ is the average concentration of the solute species and $\langle w^l \rangle^l_{FE}$ is the average solute concentration in the liquid phase. The non-linear equation (9a) is solved using a temperature-based energy solver coupled with a microsegregation model [38]. Further assuming a constant latent heat of fusion L_M, the volumetric enthalpy in Eq. (9a) can be replaced by:

$$\langle H \rangle = \langle C_p \rangle T + L_M(1 - g^s) \tag{10}$$

where $\langle C_p \rangle$ is the volumetric heat capacity. The fractions of solid and liquid, respectively g^s and g^l, verify $g^s + g^l = 1$. Eq. (9b) has two unknowns: $\langle w \rangle_{FE}$ and $\langle w^l \rangle^l_{FE}$. To solve this equation, the separation method of Voller et al. [39] is used, with taking $\langle w^l \rangle^l_{FE}$ as $\langle w^l \rangle^l_{FE} = \langle w \rangle_{FE} - \langle w \rangle^t_{FE} + \langle w^l \rangle^{l\,t}_{FE}$, where $\langle w \rangle^t_{FE}$ and $\langle w^l \rangle^{l\,t}_{FE}$ are values at the beginning of time step.

In the coupled CA-FE model, the fraction of solid is the product of the fraction of mushy zone, g^m, by the internal fraction of solid g^{sm}: $g^s = g^m \times g^{sm}$. While g^{sm} is classicaly deduced from the temperature field and $\langle w \rangle_{FE}$ using a microsegregation model (e.g., the lever rule approximation), g^m is determined onto the set of captured cells. Fraction of mushy zone g^m_ν is estimated on the CA grid for each cell ν containing a polygon growing using:

$$g^m_\nu = \frac{A_\nu - A^{capt}_\nu}{A^{max}_\nu - A^{capt}_\nu} \tag{11}$$

where A_ν is the area of the polygon at current time t, A^{capt}_ν is the area of the polygon at the time the cell has been captured and A^{max}_ν is the maximal area of the polygon. A^{capt}_ν is computed as the area of a polygon homothetic to the polygon at the numerical time of capture. In classical CA-FE models, A^{max}_ν is computed as the area of a polygon corresponding to an extension of the polygon of capture such that all neighbor cells are captured. These fractions of mushy zone g^m_ν at cell scale, computed on the CA grid, are reassigned on the FE mesh as the g^m field using shape functions of the finite element method as described in [8].

2.3.2. CAPTN-FE multiscale model special features

Fig. 3 gives a graphical representation of the CAPTN model and its coupling with the FE solution of heat and mass transfers. At a given time, the list of dendrite tip velocities $\{v_{tip,k}\}$ is computed on the PTN mesh from the FE implementation of the PTN method. These velocities are transferred to

the CA method which computes the growth of the local grain envelope, thus propagating the mushy zone on the cellular automaton grid. The cellular fraction of mushy zone is then transferred to the FE mesh where Eq. (9a) and (10) are solved to calculate the temperature field, T, the average concentration $\langle w \rangle_{FE}$ and the solid fraction, g^s. The FE fields T, g^m and $\langle w \rangle_{FE}$ are then transferred back to the

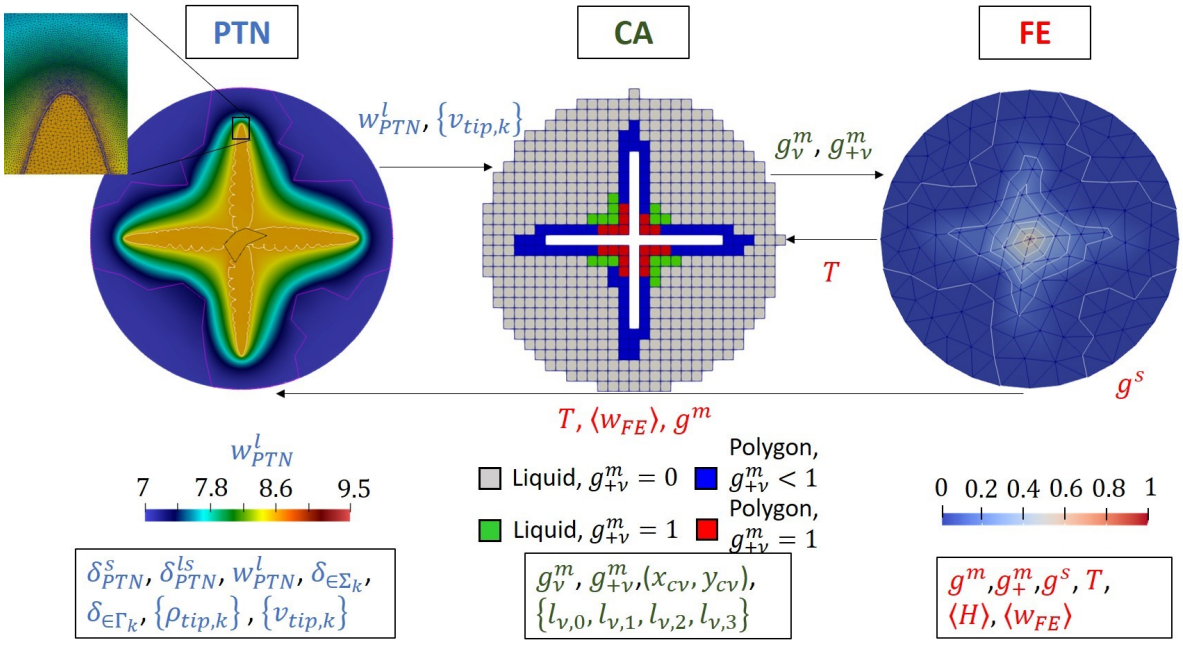

Figure 3: Illustration of the CAPTN-FE coupling for a single grain growing at the center of a disc at given time. Arrows correspond to transferred fields. PTN: w^l_{PTN} (color), edge of δ^s_{PTN} (white line), edge of area where $g^m = 0$ (pink line), edge of area where $g^m = g^m_{lim}$ (black line). Zoom: PTN mesh at a dendritic tip. CA: state of cells. The white zone in the center corresponds to deallocated cells. FE: all FE fields are displayed on separate images.

PTN mesh and used as boundary conditions for the PTN model. Indeed, the temperature field is used in the PTN model to determine the temperature at dendrite tip coordinates, which permits to deduce the corresponding equilibrium interface concentration w^{ls}. These equilibrium concentrations are therefore applied as Dirichlet conditions on nodes such that $\delta^s = 1$ for each parabola. Moreover, when the nucleation of a new polygon occurs (due to the capture of a liquid cell by one of its growing cell), dendritic branches can be too small to compute their growth velocity with the PTN method. In this case, branch velocities are computed with a growth law using Eq. (2) and the expression of the concentration field at dendrite tip given by the Ivantsov solution ($\xi = 1$ in Eq. (A.2)). Dendritic tip velocities are then noted v_{Iv}.

The evolution of the concentration field in the liquid at macroscopic scale is taken into account in the PTN model by imposing $w^l_{PTN} = \langle w \rangle_{FE}$ on nodes of the PTN mesh such that $g^m = 0$, i.e. in the liquid away from the growing grain. As explained in section 2.2.1, when all neighbors of a given cell contain a growing polygon, the cell is deallocated from the memory. Parabolae associated to its polygon are thus no longer active on the PTN mesh and the Dirichlet condition associated to their nodes is removed. As these deallocated cells have a fraction of mushy zone equal to unity, the Dirichlet condition on the PTN mesh nodes corresponding to these cells is maintained by imposing $\delta^s = 1$ for nodes such that $g^m \geq g^m_{lim}$ where g^m_{lim} is a constant threshold.

In this study, only the growth of a primary dendritic phase is modeled. Therefore, the condition for the solidification path to catch up with the microsegregation model, is that the mushy envelope of dendritic grains cover the whole domain. This corresponds to having a fraction of mushy zone equal to one for all cells to the grid. For CAPTN coupling, this necessitates to modify the definition of the fraction of mushy zone. Indeed, contrary to the CA-FE model presented in 2.3.1, each polygon branch has its own growth velocity. Moreover, for polygons created from the capture of a cell, the branch identified as the internal branch can not grow. Therefore, the methodology to compute A^{max}_ν entering Eq. (11) has to be adapted (see Appendix B) compared to the CA-FE model. Moreover, for branches close of the grain center, the solute enrichment and the decrease of solute gradients prevent branches from growing. Therefore, a large number of cells can remain in a liquid state as never being captured by a growing envelope. In practice, this corresponds to the presence of liquid in between dendrite branches but prevents from reaching $g^m = 1$ on the whole FE mesh at the end of the solidification process. To solve this difficulty, a new fraction of mushy zone $g^m_{+\nu}$ is defined on the CA grid which takes into account interdendritic cells remaining in liquid state in the calculation of the fraction of mushy zone. For this, at each time step, the PTN liquid concentration at the coordinates of liquid cells center (called $(w^l_{PTN})_\nu$) is observed and compared to the highest composition value on the PTN mesh $(w^l_{PTN})_{max}$. Cells such that $(w^l_{PTN})_\nu \geq (w^l_{PTN})_{max}(1 - \epsilon_{lim})$, where ϵ_{lim} is a constant, are set to $g^m_{+\nu} = 1$. In addition, cells containing a growing polygon are also set to $g^m_{+\nu} = 1$ as soon as all their liquid neighboring cells are set to $g^m_{+\nu} = 1$.

The extended fraction of mushy zone $g^m_{+\nu}$ and the fraction of mushy zone g^m_ν determined on the CA grid are transferred to the FE mesh. In the CAPTN-FE model, the fraction of mushy zone in Eq. (10) is replaced by g^m_+ to determine the temperature evolution and the average concentration field.

3. Application

The multiscale CAPTN-FE model is applied to an Al-Si alloy with nominal composition $w_0 = 7$ wt%Si. Properties of the alloy are reported in Table 1. The dendrite tip selection parameter σ is chosen to the

constant given by the marginal stability theory $1/(4\pi^2)$ [11]. For simplicity, material properties are assumed constant hereafter.

Table 1: Properties of the Al-7wt%Si alloy

Parameter	Variable	Value	Unit	Ref
Nominal composition	w_0	7	wt%	
Melting temperature	T_M	933.6	K	[40]
Eutectic temperature	T_{eut}	850.15	K	[40]
Segregation coefficient	k	0.13		[40]
Liquidus slope	m	-6.5	$\mathrm{K \cdot wt\%^{-1}}$	[40]
Interdiffusion coefficient in liquid	D^l	3×10^{-9}	$\mathrm{m^2 \cdot s^{-1}}$	[40]
Gibbs-Thomson coefficient	Γ^{ls}	1.96×10^{-7}	$\mathrm{K \cdot m}$	[41]
Selection parameter	σ	$1/(4\pi^2)$		[11]
Volumetric latent heat	L_M	9.5×10^8	$\mathrm{J \cdot m^{-3}}$	[42]
Volumetric heat capacity	C_p	3×10^6	$\mathrm{J \cdot m^{-3} \cdot K^{-1}}$	[42]
Thermal conductivity	κ	70	$\mathrm{W \cdot m^{-1} \cdot K^{-1}}$	[42]

3.1. Evaluation of the PTN implementation

The implementation of the PTN model itself is first evaluated. The growth of a single parabola with no truncation in a large square domain is considered for various growth conditions. For that purpose, a constant temperature T is imposed. It is related to the superstaturation, Ω defined as:

$$\Omega = \frac{w^{ls} - w_0}{w^{ls}(1-k)} \tag{12}$$

with $T = T_M + mw^{ls}$. The values of Ω are listed in Table 2. Simulations are tested over the steady state growth regime corresponding to the solution of Eq. (2) and the Ivantsov solution of the concentration field given in Eq. (A.2). Curvature radius and growth velocities corresponding to this theoretical solution are noted ρ_{Iv} and v_{Iv}. The ratio of the domain size over the expected steady state dendrite tip radius ρ_{Iv} is the same for all simulations and large enough to reach steady state. The domain size has also to be large compared to the difusion length in order to correspond to the infinite domain hypothesis of the Ivantsov solution. The parabola is initialized with a curvature radius equal to ρ_{Iv} and its velocity is equal to zero. The initial concentration field w^l_{PTN} in the liquid phase is taken equal to the Ivantsov solution (Eq. (A.2)). The time step, Δt, is adapted for the simulation as given in Table 2. The ratio $\rho_{Iv}/(v_{Iv}\Delta t)$ is the same for all simulations and chosen small enough to reach convergence. For all simulations, the mesh size in the internal part of parabola is set with $p^s = 2$.

The influence of numerical parameters on simulation results is first analyzed before discussing supersaturation effects. In these sections, average radius of curvature and growth velocities reached by the simulations are determined regarding the steady state regime.

Table 2: Simulation parameters for single parabola

Parameter	Unit	Values				
Supersaturation Ω		0.02	0.05	0.1	0.2	0.5
Curvature radius ρ_{Iv}	mm	7.3×10^{-1}	1.1×10^{-1}	2.4×10^{-2}	4.8×10^{-3}	2.9×10^{-4}
Growth velocity v_{Iv}	$\mathrm{mm \cdot s^{-1}}$	1.1×10^{-6}	4.6×10^{-5}	8.9×10^{-4}	2.1×10^{-2}	3.8
Diffusion length $l_{Iv}^D = D^l/v_{Iv}$	mm	2.8×10^{3}	6.5×10^{1}	3.4	1.4×10^{-1}	7.9×10^{-4}
Domain size	mm	4100	620	135	27	1.63
Time step Δt	s	2.4×10^{4}	88	1	8.5×10^{-3}	2.8×10^{-6}
h_{max}	mm	58.4	1.5	2	0.3	0.023

3.1.1. Influence of numerical parameters

The influence of the minimum mesh size h_{min} and of the integration zone defined by parameter a are analyzed. For this, various simulations are performed for $\Omega = 0.1$ while changing the ratios h_{min}/ρ_{Iv} and a/h_{min}. Fig. 4 a and b show two PTN meshes corresponding to two different sets of numerical parameters and Fig. 4 c and d present the ratios ρ_{tip}/ρ_{Iv} and v_{tip}/v_{Iv} obtained for various numerical parameters. Error bars correspond to the standard deviation due to fluctuation of the results inhered by finite number of elements used to compute the flux intensity factor (Eq. 6).

It is observed on Fig. 4 that the couple (ρ_{tip}, v_{tip}) converges toward the couple (ρ_{Iv}, v_{Iv}) for small values of h_{min} and large ratios a/h_{min}. Not surprisingly, the difference between (ρ_{tip}, v_{tip}) and (ρ_{Iv}, v_{Iv}) increases when the smallest mesh size h_{min} increases, whatever the value of parameter a, due to the poor description of the concentration gradient as h_{min} increases. Similarly, for a given h_{min}, the agreement between (ρ_{tip}, v_{tip}) and (ρ_{Iv}, v_{Iv}) increases with parameter a as the precision of the calculation of $\mathcal{F}$ increases with the expansion of the integration zone. Fig. 4a and b show the PTN mesh, the theoretical parabolae and the integration zone for two values of h_{min} but the same ratio a/h_{min}. For $h_{min}/\rho_{Iv} = 4$, iso-concentration lines are crossing the theoretical parabola, well illustrating the lack of precision on the physical phenomenon modeled in this situation. In practice, the smaller the minimum mesh size and the larger the integration zone parametrized by a, the longer the duration of the simulation and the higher its computational cost. A compromise has therefore to be found between the PTN model precision and the computation time.

3.1.2. Influence of supersaturation

Fig. 5 shows the evolution of ratios v_{tip}/v_{Iv} and ρ_{tip}/ρ_{Iv} with the supersaturation Ω for the same ratio $a/h_{min} = 5$ and two ratios h_{min}/ρ_{Iv}, equal to 0.1 (red) and 2 (blue). It is observed that the error on ρ_{tip} and v_{tip} drastically increases with supersaturation for $h_{min}/\rho_{Iv} = 2$, whereas these errors remain small for $h_{min}/\rho_{Iv} = 0.1$. Indeed, low values of Ω are associated to large diffusion length compared to the curvature radius ρ_{Iv} (Table 2). Therefore, for low values of Ω and for $h_{min}/\rho_{Iv} = 0.1$ and $h_{min}/\rho_{Iv} = 2$, the minimum mesh size is small compared to the diffusion length. Concentration gradients are thus

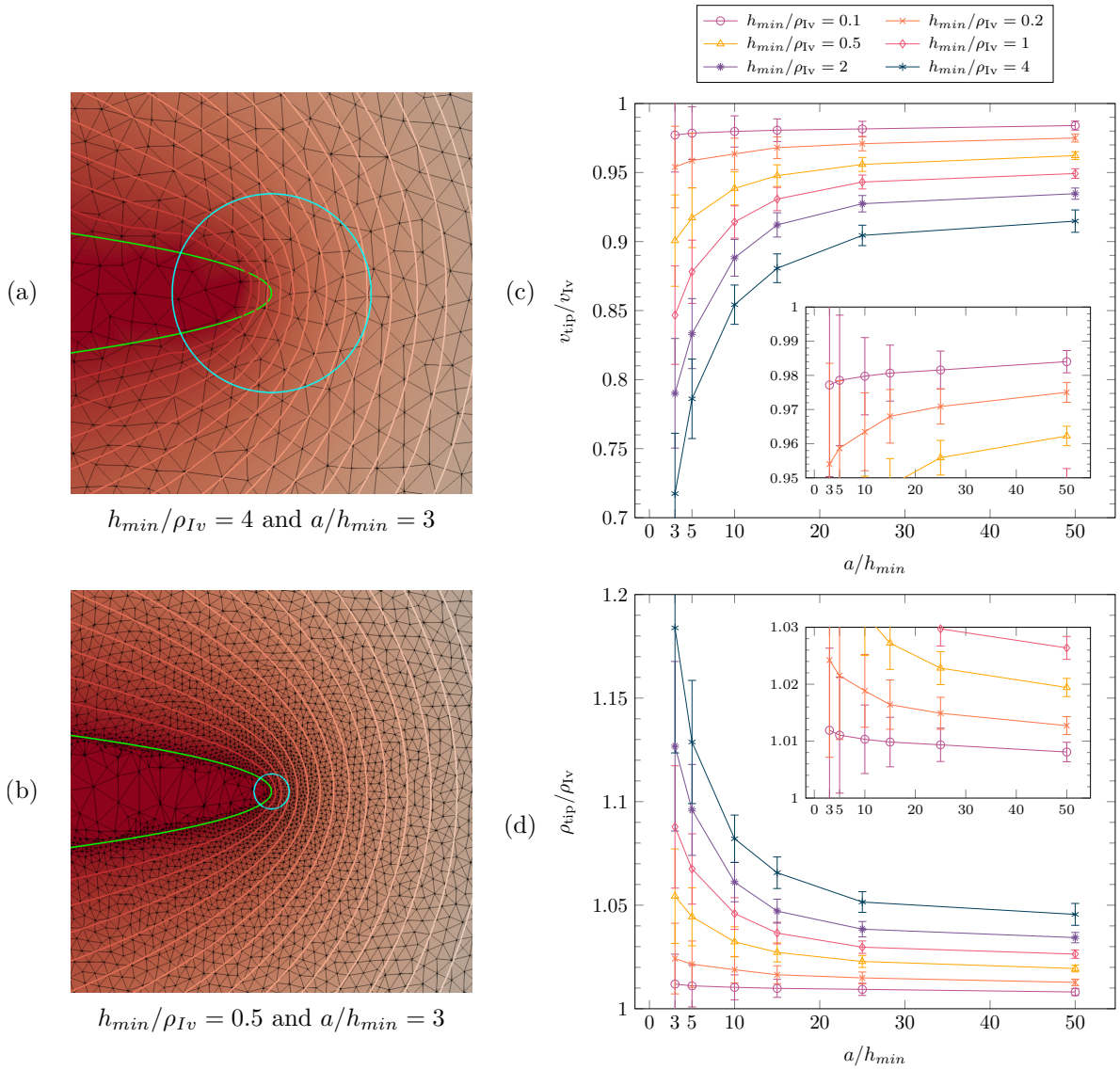

Figure 4: (a,b) FE mesh of the PTN model for two sets of numerical parameters. Theoretical parabolae are reported in green and integration zone in cyan. Iso-concentration lines are highlighted in light red (c,d) Ratios v_{tip}/v_{Iv} and ρ_{tip}/ρ_{Iv} according to a/h_{min} for various values of h_{min}/ρ_{Iv} and for $\Omega = 0.1$.

determined with a sufficient precision close to the dendrite tip, leading to correct estimation of the growth velocity. However, when Ω increases, the diffusion length decreases much faster than ρ_{Iv} and so for large values of Ω, the diffusion length is close to ρ_{Iv}. Therefore, for $h_{min}/\rho_{Iv} = 2$, the mesh is too coarse to model concentration gradients close to dendrite tip correctly.

The minimum mesh size is thus to be adjusted such that the dendrite tip and the concentration field close to the tip are well described. However, for non steady situations, it is not possible to determine tip velocity and curvature radius, especially in the transient state. The minimum mesh size, h_{min}, should

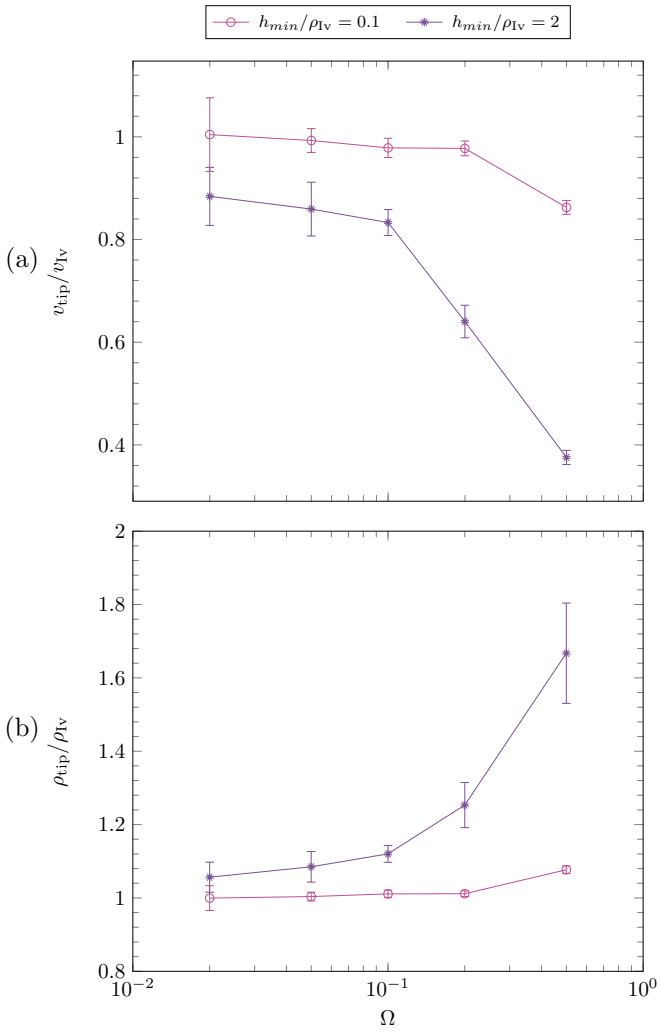

Figure 5: Ratios (a) v_{tip}/v_{Iv} and (b) ρ_{tip}/ρ_{Iv} according to the supersaturation Ω for $a/h_{min} = 5$ and (red) $h_{min}/\rho_{Iv} = 0.1$ and (blue) $h_{min}/\rho_{Iv} = 2$

therefore be adapted on tip kinetics during simulations using an adaptative remeshing strategy. This result is in agreement with previous studies on the DNN model using a finite difference implementation [43] which have shown that even if the DNN model has been developed for dendritic growth at low Peclet number, i.e. such that the curvature radius is much smaller than the diffusion length, the DNN model converges toward the Ivantsov growth law at steady state, even for large supersaturations as long as the finite difference grid is fine enough to describe concentration gradients in the vicinity of dendritic tips.

3.2. Application of the CAPTN-FE approach

The multiscale CAPTN-FE model is compared to the classical CA-FE model with simulating a single dendritic grain growing at the center of a disc of radius 0.5 mm with $< 100 >$ growth directions along

the horizontal and vertical axes as illustrated in Fig. 3. It is however outlined that this particular orientation of the grain in the plan is not a requirement and rotated grains can either be modeled using the CAPTN-FE model. The initial temperature T_{ini} is uniform and equal to 890 K. The heat is extracted at the edge of the domain with a heat transfer coefficient $h = 3\ \mathrm{W \cdot m^{-2} \cdot K^{-1}}$ and a constant external temperature $T_{ext} = 293$ K. The initial seed has branches of length 5 μm and starts to grow for a nucleation undercooling ΔT_{nucl} of 5 K. Physical and numerical parameters used in simulations are reported in Table 3.

3.2.1. Presentation of simulations

The CAPTN-FE simulation uses two different finite element meshes: the PTN mesh and the FE mesh. The latter is fixed and isotropic with size 0.15 mm. The CA grid has a cell size of $l_{CA} = 0.035$ mm. As described in section 3.1.1, the PTN mesh is an adaptive mesh. The maximal mesh size is taken as $h_{max} = 0.1$ mm and the minimum mesh size is taken as $h_{min} = \rho_{min}/10$ where ρ_{min} is the smallest radius of curvature among all parabolae in the simulation at the time of remeshing. Inside parabolae, the mesh size is set to 5 h_{min} ($p^s = 5$). To compute the flux intensity factor $\mathcal{F}$ given by Eq. (6) and to determine the growth velocity of each polygon branches, the integration parameter a is taken as $a = 10\ h_{min}$. Parabolae associated to polygon branch are finally truncated by a cylinder of radius $r_{cyl} = 0.018$ mm corresponding to half of cell size. To ensure the continuity of the Dirichlet condition on deallocated cells, the threshold g^m_{lim} is taken to 0.7 (see section 2.3.2). For fully liquid cells, the fraction of mushy zone is set to $g^m_{+\nu} = 1$ if $(w^l_{PTN})_\nu \geq (w^l_{PTN})_{max} \times 0.98$ ($\epsilon_{lim} = 0.02$).

For CA-FE simulations, physical parameters are the same as for the CAPTN-FE simulation. Polygon branches grow with a velocity v_{Iv} corresponding to the temperature and average concentration $< w_{FE} >$ at the associated cell center.

3.2.2. Simulation results

CA-FE simulation. Fig 6 presents computed FE fields and the state of CA cells in the CA-FE simulation at $t = 9.6$ s. For cells containing a polygon growing (blue cells in Fig. 6), polygon branches grow according to the solvability condition (Eq. (2)) and the Ivantsov diffusion field (Eq. (A.2) with $\xi = 1$). Thus, it accounts for the temperature at the tip (through the equilibrium condition $T = T_M + m w^{ls}$ that prescribes the interface composition w^{ls}), computed at the cell center by interpolation from the FE mesh solution. The local concentration $\langle w \rangle_{FE}$ is also accounted for. Indeed, Eq. (A.2) (with $w^l(\xi = 1)_{Iv} = w^{ls}$) is adapted to account for possible modification of the far field composition in the liquid. This is evaluated by simply replacing w_0 by $\langle w \rangle_{FE}$ in Eq. (A.2), where $\langle w \rangle_{FE}$ is also interpolated from the FE mesh solution. So in principle, if the average composition $\langle w \rangle_{FE}$ varies while the temperature remains constant, the velocity also varies. In the present simulation, the average composition given by the solution of Eq.

Table 3: Parameters of the CAPTN-FE and the CA-FE simulations

Parameter	Value	Unit
Physical parameters		
Nucleation undercooling ΔT_{nucl}	5	K
Initial temperature T_{ini}	890	K
External temperature T_{ext}	293	K
Heat transfer coefficient h	3	$\mathrm{W \cdot m^{-2} \cdot K^{-1}}$
Domain radius –	0.5	mm
Numerical parameters for the CAPTN-FE and CA-FE models		
Time step Δt	5×10^{-3}	s
Cell size l_{CA}	0.035	mm
Mesh size (FE) –	0.15	mm
Numerical parameters specific to the CAPTN-FE model		
Initial nucleus branch length –	5×10^{-3}	mm
Maximum mesh size (PTN) h_{max}	0.1	mm
Minimum mesh size (PTN) h_{min}	$(\rho_{tip})_{min}/10$	mm
Factor of solid PTN mesh size p^s	5	–
Integration parameter a	10 h_{min}	mm
Truncation radius r_{cyl}	0.018	mm
Threshold of coupling FE-PTN g^m_{lim}	0.7	–
Supersaturation threshold Ω_{lim}	0.02	–

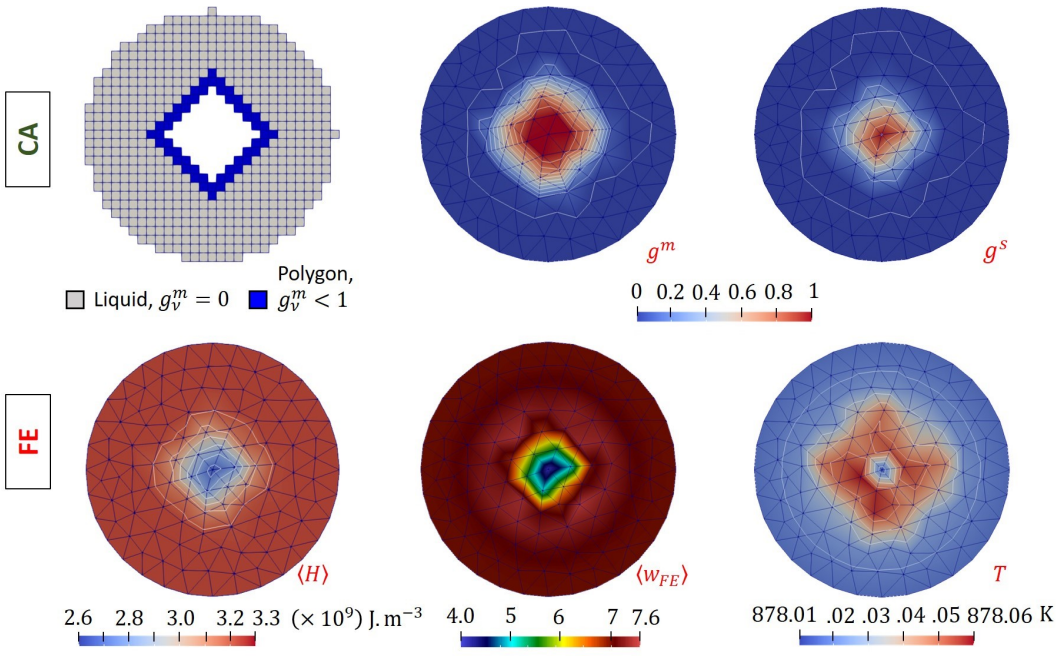

Figure 6: Snapshot at time $t = 9.6$ s of the (CA) cell state, with (white) deallocated cells and (FE) volume average variables for the CA-FE simulation.

(9b) is not found to vary significantly during the propagation of the grain envelope within the simulation domain. Similarly, the temperature remains almost uniform in the present configuration as the non dimensional Biot number is relatively low (typically less than 0.1). As a consequence, the growth velocity computed everywhere in the captured cells at the boundary with the liquid cells is almost uniform and the growth algorithm predicts the development of a squared grain envelope that finally intersects with the discoidal simulation domain.

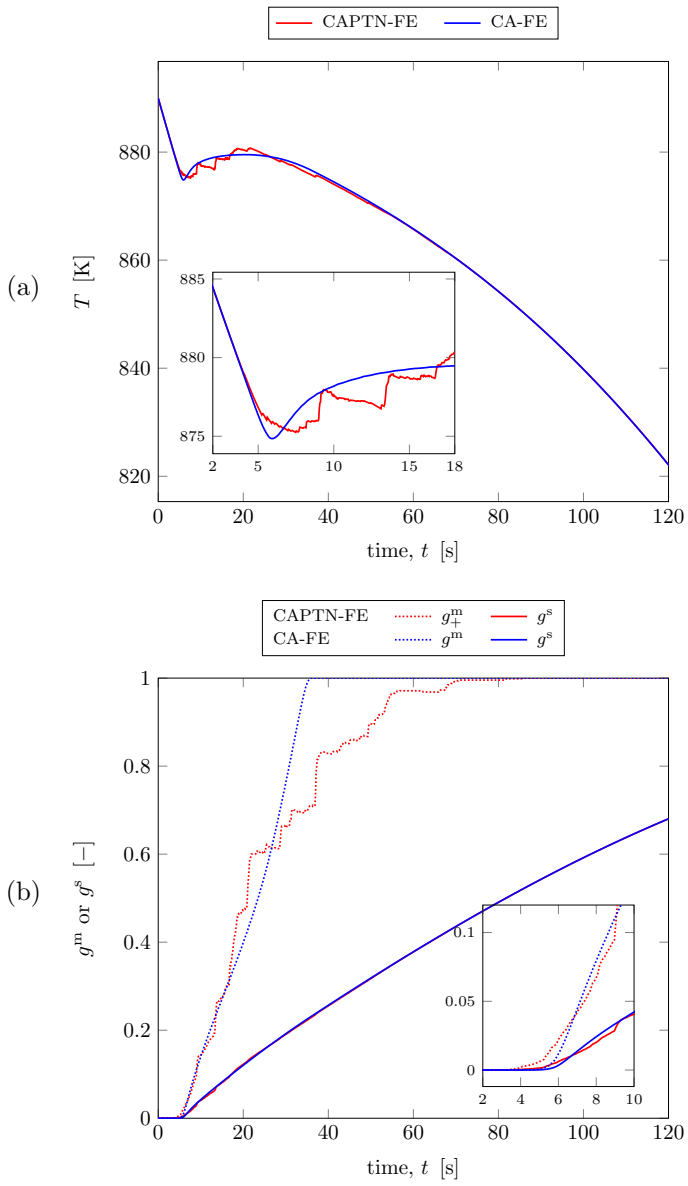

Figure 7: Average temperature (a) , fraction of mushy zone and fraction of solid (b) over time for the CAPTN-FE and the CA-FE simulations

Fig 7 presents the computed time evolution of the temperature, fraction of mushy zone and the fraction of solid averaged over the whole simulation domain. As can be observed in Fig. 7a, the average temperature starts by decreasing until $t = 6$ s. As the undercooling at the center of the domain reaches 5 K (at around $t = 3$ s), the grain starts to grow. This is illustrated by the time evolution of the length of primary branches in Fig 8a, showing an increase at around $t = 3$ s. The solid fraction g^s therefore increases in regions where $g^m \neq 0$ (see Fig 7b). As explained in section 2.3.1, this increase of g^s induces a release of latent heat and a reheat of the domain from $t = 6$ s to $t = 20$ s. This time evolution of the temperature variation due to energy conservation permits to explain the variation of the velocity of the primary branches that increases until $t = 6$ s and then decreases to reach a local minimum at $t = 20$ s (see Fig 8b). Then, as the average temperature decreases, the velocity of primary branches increases again until they reach their maximum size at $t = 29$ s. It can be observed in Fig 8a that the maximum length of primary branches is much bigger than the radius of the domain. This is allowed in the CA-FE model as polygon branches can grow over a distance larger than l_{CA} in order to capture the neighboring cells. In addition, two curves can be observed at the end of CA-FE simulations on Fig 8a and b. They correspond to an asymmetry on the cellular grid, as the grid contains one extra cell at the top and on the right of the domain compared to the bottom and left side (see Fig 6). As, for a given cell, the four polygon branches grow with the same speed, the squared grain envelope follows the elongation of primary branches and the average fraction of mushy zone reaches $g^m = 1$ at $t = 36$ s.

CAPTN-FE simulation. Fig 9 presents computed field by the combined methods: (PTN) w^l_{PTN}, (CA) g^m_+ and (FE) g^s at time $t = 9.6$ s as a result of the new hybrid model. The four branch star shape of the grain envelope is typical of high solute interactions between lateral branches. This is due to the fine resolution of the composition field w^l_{PTN} made available by the PTN mesh and used for the computation of the tip velocity provided to the CA cell polygons.

Strong variations of the concentration gradient exist in front of the dendrite at the tip of the various parabola, that is now accounted for. The polygon branches within CA cells having different speeds, only the tip of the four main dendrite branches of the grain are free to grow into the liquid along the central vertical and horizontal directions. This condition is well transferred upon successive capture of the cells, thus leading to the displayed star shape.

Cells with growing polygon (in blue in Fig. 9) are located at the boundary of the mushy zone. The liquid cells considered in the calculation of g^m_+ (in green in Fig. 9) correspond to regions with high concentration w^l_{PTN} where complete mixing of solute between branches is encountered. They are naturally first located close to the grain center. These CA cells are characterized by almost no local supersaturation. Hence, no possible propagation of the solid-liquid interface can take place in these interdendritic regions at this time, explaining why they belong to the mushy zone. Similarly, while polygons are present and continue

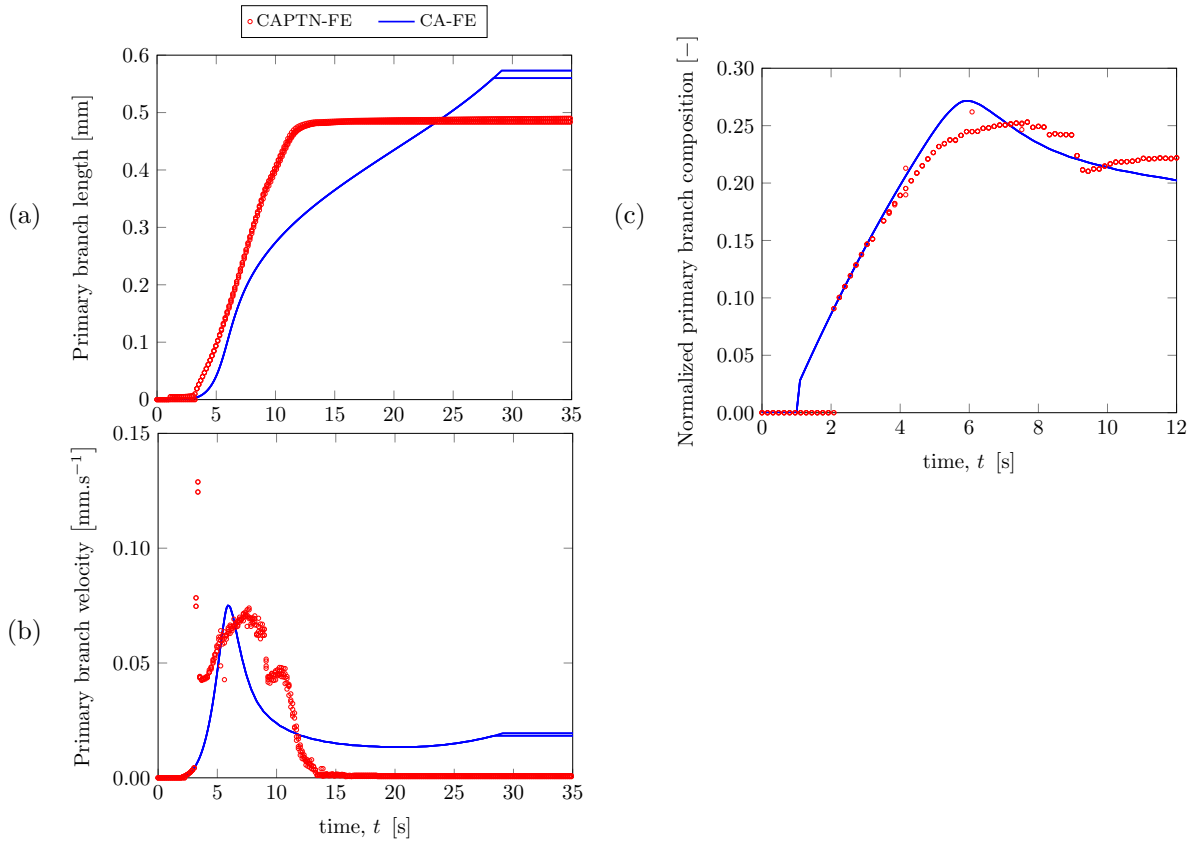

Figure 8: Length (a) velocity (b) and normalized composition (Eq. (12)) (c) of the four primary branches of the grain in the CAPTN-FE (red) and CA-FE (blue) simulations

to grow in the CA cells fully surrounded by (blue) polygon and (green) liquid cells (corresponding to $g_+^m = 1$), their growth rate is very small so they fully belong to the mushy zone (red in Fig. 9). Finally, white cells are simply deallocated regions, i.e. where associated polygon and parabolae are no longer available and needed for the calculations.

It is now worth considering the corresponding fields of the volume average FE method in Fig. 9. As explained in section 2.3.1, temperature T and solid fraction g^s are the results of conversion of the average enthalpy $\langle H \rangle$ and solute composition $\langle w \rangle_{FE}$ using the fraction of mushy zone and the microsegregation model, here simply given by the lever rule approximation. As expected, correlation is found between regions of low average enthalpy and high solid fraction. The latter naturally correspond to area where the mushy zone is developed, verified by the distribution of g^m and g_+^m. Please note that a region of low composition forms at the center of the grain, reaching an average silicon content of 4.3 $wt\%$. This is counterbalanced by liquid regions surrounding the grain envelope that exceed the nominal composition of the alloy, hence showing conservation of solute mass over the whole simulation domain. With respect to temperature, and as mentioned in the case of the CA-FE simulation, little variation is computed due to

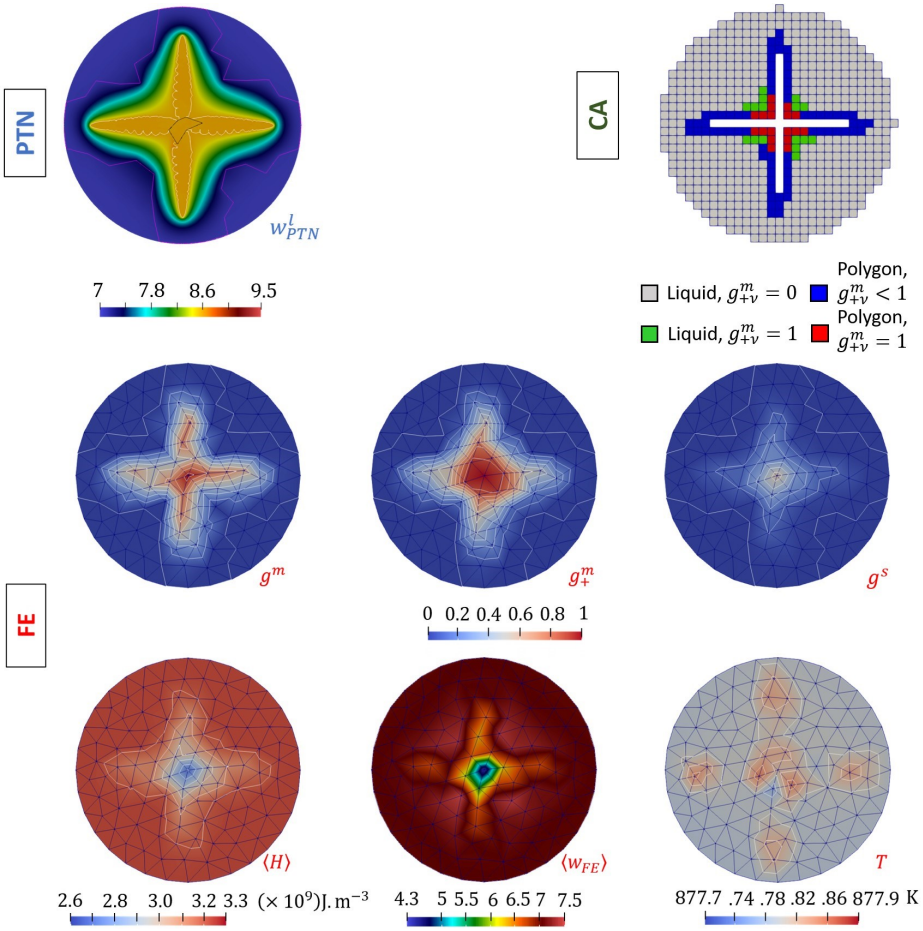

Figure 9: Snapshot at time $t = 9.6$ s of the (PTN) composition field w^l_{PTN}, (CA) mush fraction g^m_+ and cell state, with (white) deallocated cells and (FE) volume average variables.

the configuration case with low Biot number. This is why the average temperature plotted in figure 7 is well representative of the whole simulation domain. It is yet instructive to notice that locations of highest temperature indeed correspond to regions where the maximum solidification rate is expected, either due to the growth of the interface (in the vicinity of the four main tips growing along the center of the main horizontal and vertical axes) or due to the segregation of silicon at the center of the domain. Indeed, in the latter case, solute diffusion away from the central mushy zone is expected to increase the fraction of solid and hence release enthalpy that heat the system.

Fig. 10 gives the evolution of fields (PTN) w^l_{PTN}, (CA) g^m_+ and (FE) g^s at four different times during the simulation. As explained in section 2.3.2, the velocity of primary branches is first computed using the Ivantsov growth law. During this time, the liquid concentration w^l_{PTN} remains at the nominal concentration of the alloy. The transition to the PTN growth law takes place at $t = 3.05$ s. At that time, parabolae are created by an adaptation of the PTN mesh, by the update of the δ^s field and the application of the

Dirichlet condition on nodes such that $\delta^s = 1$. This sharp concentration variation close to dendrite tips induces the peak of velocity observed in Fig. 8b at $t = 3.05$ s. After this peak, the growth of primary branches is computed according to the PTN method. As the average temperature decreases, the equilibrium interfacial concentration w^{ls} increases and the concentration gradient at primary branches increases, which induces an increase of primary branches velocities. As for the CA-FE simulation, the increase of the solid fraction induces a release of latent heat and so an increase of the average temperature from $t = 7.5$ s to $t = 21$ s. As primary branches reach the edge of the domain, they get in solute interaction with the border which makes their velocity drop to zero.

Figure 8c shows the evolution of primary branches normalized compositions at the solid/liquid interface given by Eq. (12) for times such that CAPTN-FE primary branches growth velocity is not zero ($t < 12$ s). This normalized composition can be related to the temperature of primary branches during growth. It can be observed that the normalized composition and thus the temperature of primary branches is very similar between the CA-FE and CAPTN-FE simulations over time. For times between 2 and 3 s, the normalized composition is even identical between the two simulations as CAPTN-FE primary branches growth velocity is computed using the Ivantsov growth law. For times between 3.5 and 12 s, the positions of the normalized composition curves between the CAPTN-FE and the CA-FE simulation follow the same trend as average temperature curves in Fig. 7 with higher normalized composition values (lower average temperature) for the CA-FE simulation between 3.5 and 7 s and higher normalized composition values for the CAPTN-FE simulation for higher times. In addition, it is observed that for the CAPTN-FE simulation, this normalized composition is always lower than 0.25. In section 3.1.2, it has been shown that the PTN model implemented converges toward the stationary solution with a good precision in this range of supersaturation if the minimum mesh size is such that $h_{min}/\rho_{Iv} = 0.1$. Therefore, the minimum mesh size chosen for the PTN mesh in the CAPTN-FE simulation is coherent with the growth kinetics simulated.

After this time, the grain keeps growing by the increase of secondary branches (see Fig 10 PTN) and the expansion of the solute rich liquid zone (see Fig 10 CA) on the whole domain until $g_+^m = 1$ at $t = 86$ s. It is thus observed that, compared to the CA-FE model, the propagation of the fraction of mushy zone is very different in the CAPTN-FE model. In particular, it is found more difficult to reach a fraction of mushy zone equal to one in the whole domain in the CAPTN-FE model due to the decrease of dendrite tip velocities as gradients of concentration in the liquid phase decreases. When the internal part of the grain described by the CA cells is deallocated, the parabolae are no longer accessible. Consequently, the Dirichlet condition defined by the parabola of the PTN method is no longer active. It is naturally replaced by the imposed Dirichlet condition using the average composition field extracted at $g_{lim}^m = 0.7$. The corresponding region and its time evolution is made accessible by the black contours in the w_{PTN}^l field (Fig 10 PTN).

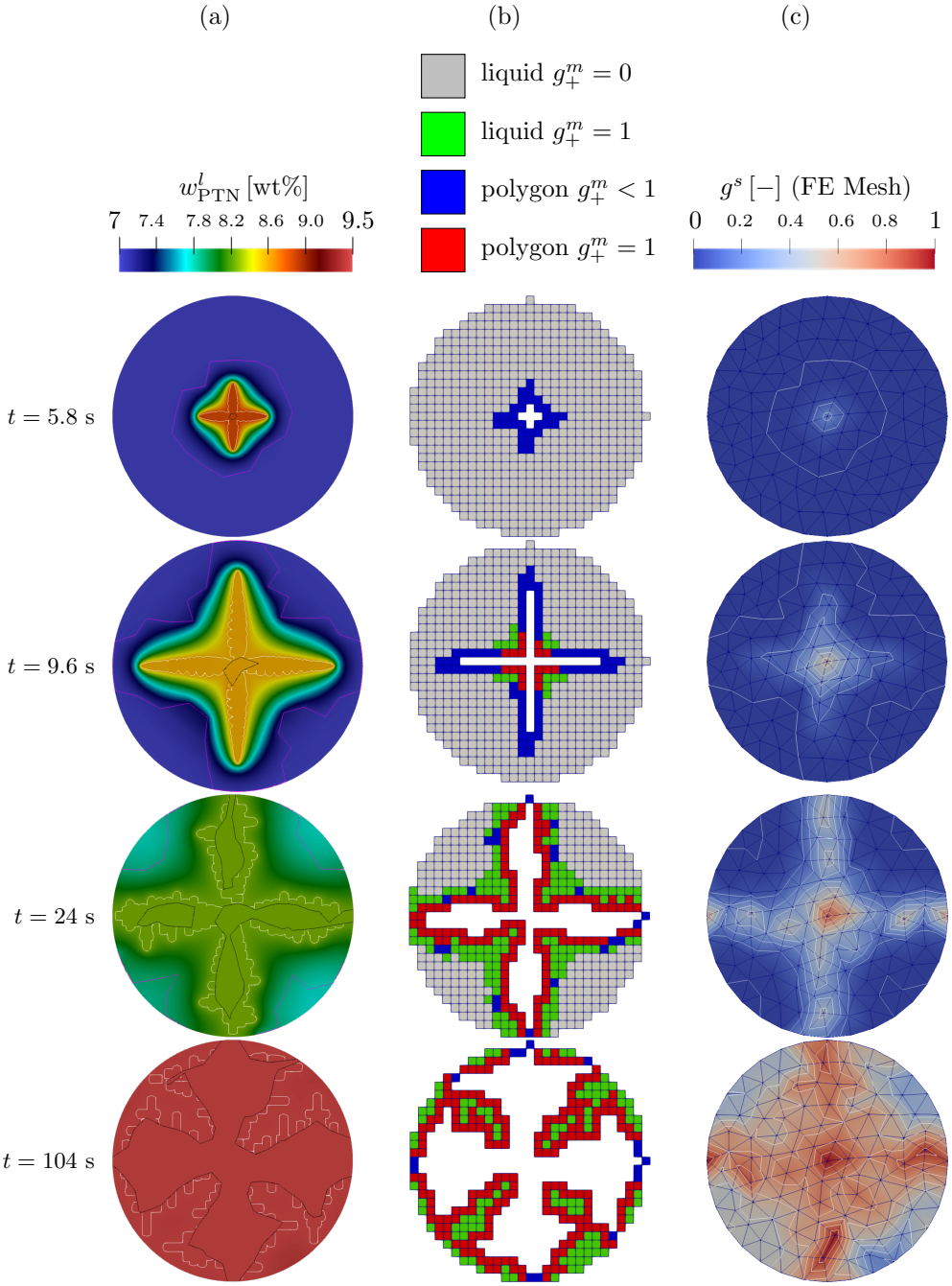

Figure 10: Evolution of the (PTN) composition field w^l_{PTN}, (CA) mush fraction g_+^m and cell state, with (white) deallocated cells and (FE) volume fraction of solid at four different times. (PTN) The white contour is the border of the Dirichlet condition using parabolae and the black line is the edge of area where $g^m = g^m_{lim}$.

It can be observed in Fig 7 that as soon as the average values of g^m (CA-FE) and g_+^m (CAPTN-FE) are equal to one, the average temperature and solid fraction of the two simulations are very similar as they

obey to the lever rule relation. Moreover, as the average temperature reaches the eutectic temperature, the average fraction of solid is close to the one associated to the eutectic temperature, 0.52, for an Al-7wt%Si alloy. However, one can clearly notice some differences between curves in Fig. 7 with successive bursts in the average fraction of mushy zone and average temperature of the CAPTN-FE simulation that are not observed for curves of the CA-FE simulation. These burst are due to the methodology used to extend the fraction of mushy zone and in particular to switch liquid cells from "out of the mushy zone" ($g^m_{+\nu} = 0$, grey cells in Fig. 10) to "part of the mushy zone" ($g^m_{+\nu} = 1$, green cells in Fig. 10) using a criterion on the concentration at the center of the cell. This methodology is explained in section 2.3.2. As can be observed in Fig 10, the area of the liquid corresponding to $g^m_{+\nu} = 1$ extends progressively from the center. Therefore, at a given time, several cells are switched from $g^m_{+\nu} = 0$ to $g^m_{+\nu} = 1$. These instantaneous changes induce the bursts observed on the average fraction of mushy zone on Fig 7b and so induce average temperature fluctuations observed on Fig 7a. An improvement of the CAPTN-FE model would therefore be to define a progressive evolution of the fraction of mushy zone for these liquid cells.

To help comparisons between the two approaches, CA-FE and CAPTN-FE simulations have been performed using the same time step and equivalent number of processors. In these numerical conditions, the duration of the CA-FE simulation was of the order of one hour and the one of the CAPTN-FE simulation was of the order of a day. The duration of the CA-FE simulation could of course be drastically reduced, in particular with using a larger time step. The large increase of the simulation time with the CAPTN-FE approach is due to the adaptive PTN mesh which has to be rebuilt frequently in order to keep track on parabolae solid/liquid interfaces. This remeshing strategy will however be optimized in future work.

4. Conclusion

In this article, a new multi-scale dendritic growth model has been presented, which couples the Cellular Automaton - Finite Element (CA-FE) solidification model to the Parabolic Thick Needle dendritic growth method. This hybrid model, implemented for now in 2D, permits to model the growth of dendritic microstructures while accounting for solutal interactions. It is fully coupled with average evolution of temperature and solute distribution at the scale of the cast part. For that purpose, the concept of mushy zone is extended compared to the classical CA-FE model while a microsegregation model is still required. Advantages with previously developed mesoscopic scale models based on the PTN approach include the possibility to conserve heat and solute mass and to benefit from previously developed model based on volume averaging, including the effect of convection at the scale of the cast part.

Despite these encouraging first results, some numerical improvements are identified which have to be handled before extending the model to 3D. This includes the computational time. While the description of the solute distribution in the vicinity of the growing dendritic microstructure clearly brings additional

physics to the model, mainly a better description of solutal interaction, at the scale of the dendrite arms, it requires additional computational resources. So improvements need to be considered, mainly in the remeshing strategy, so as to be able to simulate the whole domain of experiments [44]. As the goal of the targeted experiments is to study columnar to equiaxed transition, full coupling is yet required so heat flow surrounding equiaxed grains and its consequence on the kinetics of the dendritic microstructure are taken into account.

Acknowledgment

This work was conducted within the ESA-MAP program 'CETSOL', contract 14313/01/NL/SH.

Appendices

A. Analytical validation of the PTN model

Let's consider a single parabola of radius ρ_{tip} that models the shape of a dendrite tip close to its tip. It grows in an infinite domain of liquid at constant temperature T and a uniform composition far from the solid/liquid interface. At stationary state, the parabola adopts a constant curvature radius ρ_{tip} and a constant growth velocity v_{tip} along the x axis (see Fig. 11). We define the parabolic coordinates (ξ, η) as:

$$\begin{array}{lll} \text{Parabolic} & \rho_{tip}\xi^2 = x + \sqrt{x^2+y^2} & \rho_{tip}\eta^2 = -x + \sqrt{x^2+y^2} \\ \text{Cartesian} & x = \frac{\rho_{tip}}{2}\left(\xi^2 - \eta^2\right) & y = \rho_{tip}\xi\eta \end{array} \tag{A.1}$$

In these conditions, the concentration field should tend toward the Ivantsov solution [10] with :

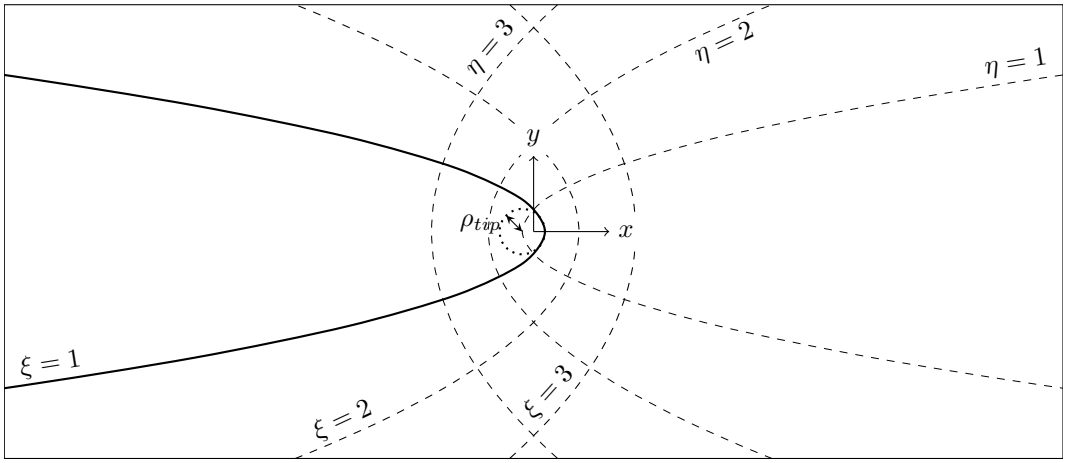

Figure 11: Parabola of curvature radius ρ_{tip} with cartesian and parabolic coordinates

$$w^l(\xi)_{Iv} = w^0 + (1-k)w^{ls}\sqrt{\pi Pe}\exp(Pe)\mathrm{erfc}(\xi\sqrt{Pe}) \tag{A.2}$$

where

$$Pe = \frac{\rho_{tip} v_{tip}}{2D^l} \tag{A.3}$$

Therefore, in Eq. (5) defining the flux intensity factor, the integral of the solute concentration gradient on the Γ' contour given in Fig. 1 can be replaced by :

$$\int_{\Gamma'} \nabla w_{Iv} \mid^{ls} \cdot \mathbf{n} \mathrm{d}\Gamma' = \int_{\Gamma'} \left(\frac{\partial w_{Iv}}{\partial \xi}\right)_{\xi=1} \mathrm{d}\Gamma' \tag{A.4}$$

The expression of w^l_{Iv} in Eq. (A.2) gives:

$$\left(\frac{\partial w_{Iv}}{\partial \xi}\right)_{\xi=1} = (1-k)w^{ls}\sqrt{\pi Pe}\exp(Pe)\frac{-2}{\sqrt{\pi}}\sqrt{Pe}\exp(-Pe) \tag{A.5}$$

Therefore, in Eq. (A.4), $\left(\frac{\partial w_{Iv}}{\partial \xi}\right)_{\xi=1}$ can be removed from the integral. The definition of the Γ' contour in Fig. 1 gives :

$$\int_{\Gamma'} \mathrm{d}\Gamma' = \sqrt{\frac{8a}{\rho_{tip}}} \tag{A.6}$$

From (A.5) and (A.6) it is obtained that:

$$\int_{\Gamma'} \nabla w_{Iv} \mid^{ls} \cdot \mathbf{n} \mathrm{d}\Gamma' = -2Pe(1-k)w^{ls}\sqrt{\frac{8a}{\rho_{tip}}} \tag{A.7}$$

Introducing Eq. (A.3) in Eq. (A.7), one can obtain:

$$\rho_{tip} v_{tip}^2 = \frac{2D^{l2}}{d_0}\left(\frac{\sqrt{d_0}}{4\sqrt{a}}\frac{-1}{(1-k)w^{ls}}\int_{\Gamma'} \nabla w_{Iv} \mid^{ls} \cdot \mathbf{n} \mathrm{d}\Gamma'\right)^2 \tag{A.8}$$

Eq. (A.8) retrieves equations (4) and (5) of the PTN model showing that the Ivantsov solution is the steady state that one should find with the present PTN model.

B. Calculation of A_ν^{max}

This appendix presents the methodology used to compute A_ν^{max} for the calculation of the fraction of mushy zone of an automaton cell using Eq. (11). In the classical CA method, the determination of A_ν^{max} corresponds to computing an elongation factor k^{max} such that all center of neighbor cells are enclosed in the polygon of cell ν. In the CAPTN-FE method, all branches of the same polygon do not have the same

speed, and if the polygon has been generated by a capture, one of the branches (the internal branch) does not grow at all. Therefore, the calculation of A_ν^{max} should be different. Fig. 12 illustrates this new method. For each of the eight neighbor cells, the algorithm analyzes if the cell could be captured by the elongation of a single branch νi of the polygon (except the internal branch) and registers the elongation factor for the branch νi. If the neighbor cell can be captured by a side of the polygon with a smaller elongation factor than for a single tip, trough the elongation of two adjacent branches, the elongation factor is registered for both branches involved. After the consideration of all neighbor cells, each branch is therefore associated to several elongation factors. The polygon corresponding to A_ν^{max} is the one associated to the maximum of elongation factors for each branch.

For example, on Fig. 12, the branch number 1 is the internal branch and the maximal elongation of branches 0 and 2 corresponds to the capture of the cell with the green circumscribed circle by the extension of side $S_\nu^0 S_\nu^2$.

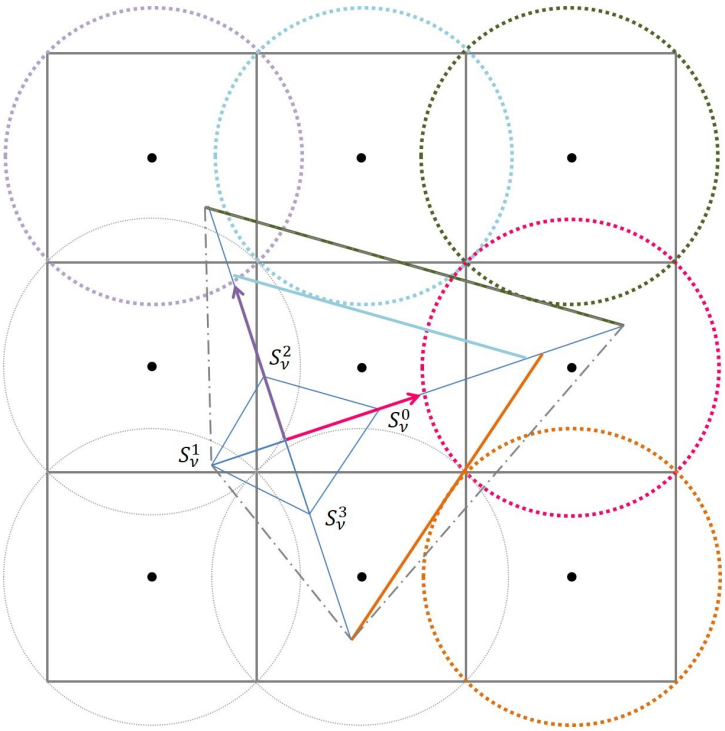

Figure 12: Initial polygon (blue) associated to the central cell ν. The branch of summit $S_{\nu 1}$ is considered as the internal branch of the polygon. Circumscribed circles of neighbor cells are represented with dotted lines. The grey polygon in dashed lines has an area A_ν^{max}. This polygon captures all neighbor cells.

References

[1] W. Kurz, M. Rappaz, and R. Trivedi. Progress in modelling solidification microstructures in metals and alloys. part ii: dendrites from 2001 to 2018. International Materials Reviews, 66(1):30–76, 2021.

[2] W. Kurz, B. Giovanolla, and R. Trivedi. Theory of microstructural development during rapid solidification. Acta Metallurgica, 34(5):823–830, 1986.

[3] M. Rappaz and Ch-A Gandin. Probabilistic modelling of microstructure formation in solidification processes. Acta metallurgica et materialia, 41(2):345–360, 1993.

[4] Ch.-A. Gandin and M. Rappaz. A coupled finite element-cellular automaton model for the prediction of dendritic grain structures in solidification processes. Acta metallurgica et materialia, 42(7):2233–2246, 1994.

[5] Ch.-A. Gandin and M. Rappaz. A 3d cellular automaton algorithm for the prediction of dendritic grain growth. Acta Materialia, 45(5):2187–2195, 1997.

[6] J. A. Dantzig and M. Rappaz. Solidification. 2016.

[7] Ch.-A. Gandin, J.-L. Desbiolles, M. Rappaz, and P. Thevoz. A three-dimensional cellular automation-finite element model for the prediction of solidification grain structures. Metallurgical and Materials Transactions A, 30(12):3153–3165, 1999.

[8] T. Carozzani, H. Digonnet, M. Bellet, and Ch.-A. Gandin. 3d cafe simulation of a macrosegregation benchmark experiment. Materials Science and Engineering, 33(1):12087–12096, 2012.

[9] T. Carozzani, Ch.-A. Gandin, H. Digonnet, M. Bellet, K. Zaidat, and Y. Fautrelle. Direct simulation of a solidification benchmark experiment. Metallurgical and Materials Transactions A, 44(2):873–887, 2013.

[10] G.P. Ivantsov. Temperature field around a spherical, cylindrical, and needle-shaped crystal, growing in a pre-cooled melt. Dokl. Akad. Nauk SSSR, 58(4):567 – 569, 1947.

[11] J.S. Langer and H. Müller-Krumbhaar. Theory of dendritic growth—i. elements of a stability analysis. Acta Metallurgica, 26(11):1681–1687, 1978.

[12] Ch.-A. Gandin, G. Guillemot, B. Appolaire, and N.T. Niane. Boundary layer correlation for dendrite tip growth with fluid flow. Materials Science and Engineering: A, 342(1-2):44–50, 2003.

[13] G. Guillemot, Ch.-A. Gandin, and H. Combeau. Modeling of macrosegregation and solidification grain structures with a coupled cellular automaton—finite element model. ISIJ international, 46(6):880–895, 2006.

[14] A. Saad, Ch.-A. Gandin, M. Bellet, O. Shevchenko, and S. Eckert. Simulation of channel segregation during directional solidification of in—75 wt pct ga. qualitative comparison with in situ observations. Metallurgical and Materials Transactions A, 46(11):4886–4897, 2015.

[15] J. Ni and C. Beckermann. A volume-averaged two-phase model for transport phenomena during solidification. Metallurgical Transactions B, 22(3):349–361, 1991.

[16] C.Y. Wang and C. Beckermann. A multiphase solute diffusion model for dendritic alloy solidification. Metallurgical and Materials Transactions A, 24(12):2787–2802, 1993.

[17] T. Koshikawa, Ch.-A. Gandin, M. Bellet, H. Yamamura, and M. Bobadilla. Computation of phase transformation paths in steels by a combination of the partial-and para-equilibrium thermodynamic approximations. ISIJ international, 54(6):1274–1282, 2014.

[18] W. Wang, P.D. Lee, and M. Mclean. A model of solidification microstructures in nickel-based superalloys: predicting primary dendrite spacing selection. Acta materialia, 51(10):2971–2987, 2003.

[19] L. Beltran-Sanchez and D.M. Stefanescu. Growth of solutal dendrites: a cellular automaton model and its quantitative capabilities. Metallurgical and Materials Transactions A, 34(2):367–382, 2003.

[20] A. Kao, I. Krastins, M. Alexandrakis, N. Shevchenko, S. Eckert, and K. Pericleous. A parallel cellular automata lattice boltzmann method for convection-driven solidification. JOM, 71(1):48–58, 2019.

[21] K Reuther and M Rettenmayr. Perspectives for cellular automata for the simulation of dendritic solidification–a review. Computational materials science, 95:213–220, 2014.

[22] A. Karma and W.J. Rappel. Quantitative phase-field modeling of dendritic growth in two and three dimensions. Physical Review E, 57(4):4323, 1998.

[23] T. Shimokawabe, T. Aoki, T. Takaki, T. Endo, A. Yamanaka, N. Maruyama, A. Nukada, and S. Matsuoka. Peta-scale phase-field simulation for dendritic solidification on the tsubame 2.0 supercomputer. In Proceedings of 2011 International Conference for High Performance Computing, Networking, Storage and Analysis, pages 1–11, 2011.

[24] D. Tourret and A. Karma. Growth competition of columnar dendritic grains: A phase-field study. Acta Materialia, 82:64–83, 2015.

[25] A. Pineau, G. Guillemot, D. Tourret, A. Karma, and Ch.-A. Gandin. Growth competition between columnar dendritic grains–cellular automaton versus phase field modeling. Acta Materialia, 155:286–301, 2018.

[26] D. Tourret and A. Karma. Multiscale dendritic needle network model of alloy solidification. Acta materialia,

61(17):6474–6491, 2013.

[27] D. Tourret and A. Karma. Three-dimensional dendritic needle network model for alloy solidification. Acta Materialia, 120:240–254, 2016.

[28] P.-A. Geslin, C.-H. Chen, A.M. Tabrizi, and A. Karma. Dendritic needle network modeling of the columnar-to-equiaxed transition. part i: two dimensional formulation and comparison with theory. Acta Materialia, 202:42–54, 2021.

[29] C.-H. Chen, A.M. Tabrizi, P.-A. Geslin, and A. Karma. Dendritic needle network modeling of the columnar-to-equiaxed transition. part ii: three dimensional formulation, implementation and comparison with experiments. Acta Materialia, 202:463–477, 2021.

[30] Y. Souhar, V.F. De Felice, C. Beckermann, H. Combeau, and M. Založnik. Three-dimensional mesoscopic modeling of equiaxed dendritic solidification of a binary alloy. Computational Materials Science, 112:304, 2016.

[31] A. Viardin, M. Založnik, Y. Souhar, M. Apel, and H. Combeau. Mesoscopic modeling of spacing and grain selection in columnar dendritic solidification: Envelope versus phase-field model. Acta Materialia, 122:386, 2017.

[32] A. Olmedilla, M. Založnik, and H. Combeau. Quantitative 3d mesoscopic modeling of grain interactions during equiaxed dendritic solidification in a thin sample. Acta Materialia, 173:249, 2019.

[33] J.S. Langer. Dendrites, viscous fingers, and the theory of pattern formation. Science, 243(4895):1150–1156, 1989.

[34] A. Barbieri and J.S. Langer. Predictions of dendritic growth rates in the linearized solvability theory. Physical Review A, 39(10):5314, 1989.

[35] F. Alauzet, P.J. Frey, and George P. Anisotropic mesh adaptation for rayleigh-taylor instabilities. ECCOMAS 2004 - European Congress on Computational Methods in Applied Sciences and Engineering, 01 2004.

[36] Ch.-A. Gandin, R.J. Schaefer, and M. Rappaz. Analytical and numerical predictions of dendritic grain envelopes. Acta materialia, 44(8):3339–3347, 1996.

[37] M. Rappaz, M. Bellet, and M. Deville. Modélisation numérique en science et génie des matériaux, volume 10. PPUR presses polytechniques, 1998.

[38] A. Saad, Ch.-A. Gandin, and M. Bellet. Temperature-based energy solver coupled with tabulated thermodynamic properties–application to the prediction of macrosegregation in multicomponent alloys. Computational Materials Science, 99:221 – 231, 2015.

[39] V. R. Voller, A. D. Brent, and C. Prakash. The modelling of heat, mass and solute transport in solidification systems. International Journal of Heat and Mass Transfer, 32(9):1719–1731, 1989.

[40] W. Kurz and D.J. Fisher. Fundamentals of solidification. 1989.

[41] M. Gündüz and J.D. Hunt. The measurement of solid-liquid surface energies in the al-cu, al-si and pb-sn systems. Acta Metallurgica, 33(9):1651 – 1672, 1985.

[42] R.D. Pehlke, A. Jeyarajan, and H. Wada. Summary of thermal properties for casting alloys and mold materials. NASA STI/Recon Technical Report N, 83, 1982.

[43] D. Tourret, M.M. Francois, and A.J. Clarke. Multiscale dendritic needle network model of alloy solidification with fluid flow. Computational Materials Science, 162:206–227, 2019.

[44] G. Zimmermann, L. Sturz, B. Billia, N. Mangelinck-Noël, D.R. Liu, H. Nguyen Thi, N. Bergeon, Ch.-A. Gandin, D.J. Browne, C. Beckermann, et al. Columnar-to-equiaxed transition in solidification processing of alsi7 alloys in microgravity the cetsol project. In Materials Science Forum, volume 790, pages 12 – 21. Trans Tech Publ, 2014.